Shear Strength of Composite Circular Reinforced Concrete–Filled Steel Tubes

Hadi Kenarangi, S.M.ASCE[1]; and Michel Bruneau, F.ASCE[2]

Abstract: The shear strength of composite circular concrete-filled steel tube (CFST) and reinforced concrete–filled steel tube (RCFST) structural members was investigated using finite-element analysis and existing test data. Results showed how a compression strut develops in concrete infill under shear load in the presence of low shear spans and provided the basis for proposing a mechanics-based shear strength equation for those composite members. The proposed equation quantifies the contribution of that strut to total strength as a function of shear span and accounts for the interactions between the steel tube and the concrete infill. The effectiveness of the proposed equation was compared with shear test data from the existing literature and was found to be safe; it accurately captures the contribution of the steel tube to the total strength and conservatively estimates that of the concrete. **DOI: 10.1061/(ASCE)ST.1943-541X.0002456.**

Author keywords: Concrete-filled steel tubes; Shear strength; Composite; Drilled shafts; Finite-element model; Compression strut; Mechanics-based equation.

Introduction and Background

Concrete-filled steel tubes (CFSTs) have been used in seismic-resistant buildings and bridges. Several studies have proved the desirable seismic performance of these members under flexure (Hajjar 2000; Marson and Bruneau 2004; Han and Yang 2005; Hajjar et al. 2013). Findings from these studies have supported the development of design equations to calculate the plastic strength of such members under combined bending and axial load (e.g., Bruneau and Marson 2004; Leon et al. 2007; Roeder et al. 2010; Lai et al. 2014). The flexural behavior of CFSTs with internal reinforcement has also been studied in recent years (Brown 2013; Moon et al. 2013; Bruneau et al. 2018), and equations haven been proposed to calculate their strength (Moon et al. 2013; Bruneau et al. 2018). A CFST with internal reinforcement is referred to as reinforced concrete–filled steel tubes (RCFSTs).

While the flexural behavior of CFSTs has been widely researched experimentally and analytically, there is considerably less experimental and analytical knowledge on the shear behavior of these members. In most applications, a conservative estimate of shear strength (i.e., neglecting the contribution of concrete) is sufficient because shear is rarely a governing limit state for CFST members. However, in some instances, better knowledge of this shear strength is desirable. For example, bridge single shaft foundations constructed as RC shafts cast in a permanent steel casing embedded in the soil sometimes span across a liquefiable soil layer; in this case, seismically induced lateral spreading of the soil above a thin liquefiable layer can introduce severe shear loading over a short length of the RCFST shaft height (i.e., the shaft crossing the liquefiable layer is subject to double curvature bending and resulting high shear). In this case, the shear strength of the drilled shaft can become a significant consideration in determining the final dimensions of the drilled shaft.

The majority of the tests on the shear strength of composite CFSTs and RCFSTs have been conducted using three- or four-point bending setups with simple end supports and under monotonic loadings (Qian et al. 2007; Xu et al. 2009; Xiao et al. 2012; Roeder et al. 2016). These test setups generate single curvature deflection along the member and, depending on the distance of the supports from each other, can produce flexure, flexure-shear, and shear dominant failures for large to short support distances, respectively.

More representative of the loading likely to be experienced by drilled shafts subject to the aforementioned liquefaction condition, or even of building columns for which the shear limit state governs the flexural one (such as in panel zones or when braces have small eccentricities at connections), or other applications, some tests have considered specimens subject to double curvature deflection rather than a single curvature. Monotonic double curvature shear tests on small-diameter CFSTs [11.9 cm (4.7 in.) diameter] were performed by Ye et al. (2016) using a three-point bending setup and fixed support conditions at both ends. Cyclic double curvature tests were performed by Nakahara and Tsumura (2014) on 16.5 cm (6.5 in.)-diameter CFSTs and Bruneau et al. (2018) on larger-diameter CFSTs and RCFSTs.

Bruneau et al. (2018) tested seven shear specimens, including two CFSTs with 32.4- (12.75-) and 40.6 cm (16 in.) diameters, four 32.4 cm (12.75 in.)-diameter RCFSTs with various reinforcing configurations, and a hollow 32.4 cm (12.75 in.)-diameter steel tube. Shear specimens were tested in a pantograph device under cyclic loading. The pantograph test setup made it possible to test the specimens by introducing a double curvature deformation. Considering the properties of the steel tube and concrete, the ratio of shear span length to diameter of all specimens were chosen to have shear-dominant yielding and failure. The existing shear test data are summarized in Table 1. In this table, D is the diameter of the steel tube, a is the clear span between the supports for single curvature test setups and half of this value for the double curvature test setups, P is the applied axial compressive load, and P_0 is the summation of yield strength of the steel tube and crushing capacity of the concrete ignoring buckling.

[1]Graduate Research Assistant, Dept. of Civil, Structural, and Environmental Engineering, Univ. at Buffalo, Buffalo, NY 14260 (corresponding author). ORCID: https://orcid.org/0000-0002-8750-7722. Email: hadikena@buffalo.edu

[2]Professor, Dept. of Civil, Structural, and Environmental Engineering, Univ. at Buffalo, Buffalo, NY 14260. Email: bruneau@buffalo.edu

Note. This manuscript was submitted on February 6, 2018; approved on April 25, 2019; published online on October 31, 2019. Discussion period open until March 31, 2020; separate discussions must be submitted for individual papers. This paper is part of the ***Journal of Structural Engineering***, © ASCE, ISSN 0733-9445.

Table 1. Summary of existing test data on shear strength of RCFST members

Reference	Test setup	Loading type	Diameter range	$\frac{a}{D}$ range	$\frac{P}{P_0}$ range
Bruneau et al. (2018)	Double curvature	Cyclic pantograph	30.5 cm (12 in.) and 40.6 cm (16 in.)	0.4	0
Roeder et al. (2016)	Single curvature	Monotonic four point bending	50.8 cm (20 in.)	0.25–1.0	0, 0.085
Ye et al. (2016)	Double curvature	Monotonic three point bending	11.9 cm (4.7 in.)	0.15–0.75	0–0.73
Nakahara and Tsumura (2014)	Double curvature	Cyclic pantograph	16.5 cm (6.5 in.)	0.5	0–0.4
Xiao et al. (2012)	Single curvature	Monotonic three-point bending	16.5 cm (6.5 in.)	0.14–1.0	0–0.62
Xu et al. (2009)	Single curvature	Monotonic three-point bending	14 cm (5.5 in.)	0.1–0.5	0
Qian et al. (2007)	Single curvature	Monotonic three-point bending	19.6 cm (7.7 in.)	0.1–0.3	0–0.77

It is important for design purposes to understand the physical behavior of composite RCFSTs subject to shear and to develop design equations that adequately capture the respective contribution of the steel and concrete of the RCFST to its total shear strength (contribution of internal reinforcement is not considered here for reasons described later). Design equations that are more anchored in the actual physical behavior of a structural member provide more confidence in the design. For example, overestimating the strength of one component could also result in an unexpected failure should that component become dominant in providing the total shear strength of that member.

The work discussed here (1) presents an assessment of the existing shear equations in AASHTO LRFD Bridge Design Specifications (AASHTO BDS) (AASHTO 2014) and the Washington Department of Transportation Bridge Design Manual LRFD (WSDOT BDM) (WSDOT 2018) using the finite-element analyses of the tests done by Bruneau et al. (2018) and identifies the shortcomings of those equations, (2) presents results from finite-element analyses done to understand the mechanics that govern the shear strength of composite RCFSTs, and (3) proposes a mechanics-based shear strength equation for composite CFST members based on those analyses. The proposed shear strength formula is compared to the existing shear test data. The study presented here was done using the results of finite-element analyses conducted using finite-element models validated by Bruneau et al. (2018).

Shear Strength Equations in AASHTO and DOTs

The existing shear strength equations implemented in AASHTO BDS (AASHTO 2014) and AISC 360 (AISC 2016) and those from the WSDOT BDM (WSDOT 2018) are presented in what follows. The shear strength experimentally obtained by Bruneau et al. (2018) is then compared with those calculated using the equations from AASHTO BDS (AASHTO 2014) and WSDOT BDM (WSDOT 2018).

The AASHTO BDS (AASHTO 2014) does not directly provide an equation to calculate the shear strength of composite RCFSTs. However, it provides equations for the shear strength of a circular steel tube and concrete cross sections, in Sections 6.12.1.2.3c and 5.8.3.3, respectively. These equations are as follows:

$$V_{yst(\text{AASHTO})} = 0.5F_{cr}A_s \quad 6.12.1.2.3c\text{-}1 \tag{1}$$

where $V_{yst(\text{AASHTO})}$ = shear strength of circular steel tube; and F_{cr} = shear buckling resistance taken as the larger of either

$$F_{cr1} = \frac{1.60E_s}{\sqrt{\frac{L_v}{D}}\left(\frac{D}{t}\right)^{\frac{5}{4}}} \le 0.58F_y \quad 6.12.1.2.3c\text{-}2 \tag{2}$$

or

$$F_{cr2} = \frac{0.78E_s}{\left(\frac{D}{t}\right)^{\frac{3}{2}}} \le 0.58F_y \quad 6.12.1.2.3c\text{-}3 \tag{3}$$

in which A_s = area of steel tube cross section based on design wall thickness; E_s = modulus of elasticity of the steel; F_y = yield strength of steel tube; D = outside diameter of steel tube; L_v = distance between points of maximum and zero shear; and t = design wall thickness taken to be equal to 0.93 times the nominal wall thickness for ERW round HSS. Note that in a CFST, the concrete fill provides support against buckling of the steel tube, and therefore F_{cr} is taken as $0.58F_y$ for these sections. For the concrete, the shear strength can be calculated as

$$V_{c(\text{AASHTO})}(\text{MPa}) = 0.01286\beta A_c\sqrt{f'_c(\text{MPa})} \quad 5.8.3.3\text{-}3 \tag{4}$$

where β = taken to be equal to 2.0; f'_c = uniaxial compressive strength of concrete (MPa); A_c = area of concrete section (cm^2). Based on comments provided by practicing engineers and using engineering judgment, the composite shear strength can be calculated by summing the shear strengths of the steel tube and the concrete as

$$V_{n(\text{AASHTO})} = V_{yst(\text{AASHTO})} + V_{c(\text{AASHTO})} \tag{5}$$

However, calculating the shear capacity of CFSTs by simply adding the shear strengths of steel and concrete parts without considering any interaction between those parts may be overly conservative in many instances (Roeder et al. 2016; Bruneau et al. 2018). The shear strength of circular filled composite members given by AISC 360 (AISC 2016), Chapter I, is that of the (1) yield shear strength of the steel tube alone, (2) the available shear strength of the reinforced concrete portion alone, or (3) the yield shear strength of the steel tube plus the shear strength of the reinforcing steel. The strength given by AISC 360 (AISC 2016) is more conservative compared to Eq. (5). Underestimating the shear strength of the shaft could result in inefficient material use and a significant increase in construction costs.

Improving on these approaches, the WSDOT BDM (2018) includes an updated formula for the shear capacity of RCFSTs that is based on research done by Roeder et al. (2016). This formula was developed according to a mathematical fit on the tests they performed and test data available at the time as well as finite-element analysis results.

Eq. (7.10.2-15) of the WSDOT BDM (WSDOT 2018) calculates the shear strength of CFST and RCFST as two times the shear yield strength of the steel tube plus the shear strength of the concrete fill calculated similarly to Eq. (4) using a β factor equal to 3. This equation neglects the contribution of the internal reinforcement and does not account for the influence of the axial load. The WSDOT BDM (WSDOT 2018) also allows the use of another equation proposed in Roeder et al. (2016) as an alternative to Eq. (7.10.2-15). The proposed equation by Roeder et al. (2016) accounts for the internal reinforcing and the axial load and calculates the nominal shear strength of CFST and RCFST as follows:

$$V_{n(\text{WSDOT})} = 2V_{st(\text{WSDOT})} + V_{srl(\text{WSDOT})} + \eta V_{c(\text{WSDOT})} \tag{6a}$$

In this equation the total composite shear strength is the summation of two times the shear yield strength resisted by the steel tube [$2V_{st(\mathrm{WSDOT})}$], the shear strength of the internal reinforcing [$V_{srl(\mathrm{WSDOT})}$], and the concrete fill [$\eta V_{c(\mathrm{WSDOT})}$]. Each of these contributions is calculated as follows:

$$V_{st(\mathrm{WSDOT})} = 0.6F_{yt}(0.5A_{st}) \tag{6b}$$

$$V_{srl(\mathrm{WSDOT})} = 0.6F_{yrl}(0.5A_{srl}) \tag{6c}$$

$$\eta = 5\left(1 + 5\frac{P}{P_0}\right) \le 10 \tag{6d}$$

$$V_{c(\mathrm{WSDOT})} = 0.01286A_c\,(\mathrm{cm}^2)\sqrt{f'_c(\mathrm{MPa})} \tag{6e}$$

In the preceding equations, F_{yt} and A_{st} are the yield stress and cross-sectional area of the steel tube, respectively, and F_{yrl} and A_{srl} are the yield stress and total cross-sectional area of the longitudinal reinforcement, respectively. Additionally, f'_c and A_c are the uniaxial compressive strength and cross-sectional area of the concrete infill, respectively, and P and P_0 are the externally applied axial load and the crushing capacity of the RCFST cross section ignoring buckling, respectively. The WSDOT BDM (WSDOT 2018) Eq. (7.10.2-15) and the alternative equation proposed by Roeder et al. (2016) are similar in terms of calculating the contribution of the steel tube. However, the alternative equation accounts for a higher contribution of the concrete as well as the influence of the axial load. The alternative equation was considered as WSDOT BDM (WSDOT 2018) in the following comparisons.

As an example of how the predicted strengths from AASHTO BDS (AASHTO 2014) and WSDOT BDM (WSDOT 2018) compare to experimental results, Table 2 presents the properties of the specimens tested by Bruneau et al. (2018), the experimentally obtained maximum shear strength, and the corresponding shear strengths calculated from AASHTO BDS (AASHTO 2014) and WSDOT BDM (2018) equations. As presented in this table, the AASHTO BDS (AASHTO 2014) equations give conservative values for the shear strength of the tested CFSTs and RCFSTs. The shear strengths calculated by the WSDOT BDM (WSDOT 2018) equation for the filled specimens were closer to the experimentally obtained shear strength values.

Fig. 1 shows results from the cyclic finite-element analysis of Specimen SH4. In this figure, the shear force respectively carried by the steel tube and the concrete of the specimen is plotted separately and is compared to the corresponding values calculated from the AASHTO BDS (AASHTO 2014) and WSDOT BDM (WSDOT 2018) equations in Figs. 1(a and b), respectively. Also, the points where the first yield happened and the maximum experimental shear strength was reached are identified in this figure. The first yield was determined by the point where the first yield occurred on the steel tube. The yielding happened at the middle of the cross section where the shear stress is at its maximum. The shear force carried by the steel tube and the concrete was calculated by cutting a section at the midheight of the member and integrating the shear force over the steel tube and concrete cross section, respectively. The summation of these contributions is equal to the total shear carried by the composite cross section.

The LS-Dyna (LSTC 2013) model of the shear specimen and test setup is schematically shown in Fig. 2. To include the effects

Table 2. Test specimens of Bruneau et al. (2018) properties, results, and comparison with existing shear strength equations

Specimen	OD (cm)	a (cm)	$\frac{a}{OD}$	t (cm)	$\frac{D}{t}$	f'_c, (MPa)	E_c (MPa)	f_y (MPa)	Reinforcing (Grade 60 ksi)	$V_{\exp}$ (kN)	$V_{n(\mathrm{AASHTO})}$ (kN)	$V_{n(\mathrm{WSDOT})}$ (kN)	$\frac{V_{\exp}}{V_{n(\mathrm{AASHTO})}}$	$\frac{V_{\exp}}{V_{n(\mathrm{WSDOT})}}$
SH2 (CFST)	40.6	16.5	0.41	0.6	68.8	20	19,009	351.6	No reinforcement	1,943.9	840.7	1,783.7	2.31	1.09
SH4 (CFST)	32.4	12.7	0.39	0.6	54.8	31	23,677	399.9	No reinforcement	1,761.5	756.2	1,588.0	2.33	1.11
SH5 (RCFST)	32.4	12.7	0.39	0.6	54.8	31	23,677	399.9	Longitudinal 6#4 (ρ_s =1%) no transverse	1,765.9	756.2	1,685.9	2.34	1.05
SH6 (RCFST)	32.4	12.7	0.39	0.6	54.8	31	23,677	399.9	Longitudinal 6#6 (ρ_s = 2.2%) no transverse	1,841.6	756.2	1,801.5	2.44	1.02
SH7 (RCFST)	32.4	12.7	0.39	0.6	54.8	31	23,677	399.9	Longitudinal 6#4 spiral #3@10.2 cm	1,810.4	756.2	1,685.9	2.39	1.07
SH1R (RCFST)	32.4	12.7	0.39	0.6	54.8	31	23,677	399.9	Longitudinal 6#4 spiral #3@7.6 cm	1,797.1	756.2	1,685.9	2.38	1.07

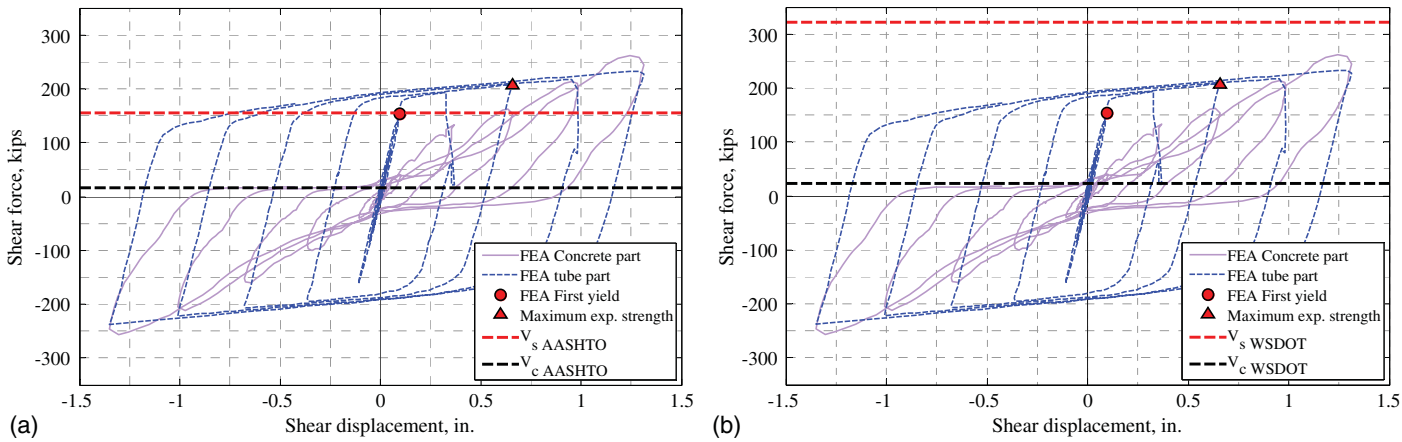

Fig. 1. Comparison of component shear forces with (a) AASHTO BDS (AASHTO 2014); and (b) WSDOT BDM (WSDOT 2018).

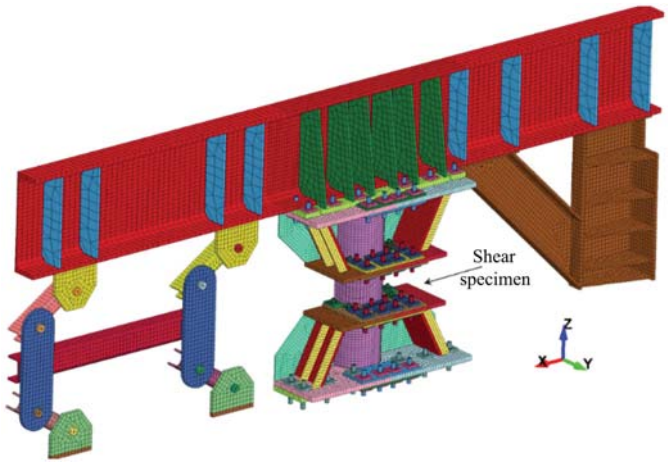

Fig. 2. Scheme of the developed LS-Dyna finite-element model for shear tests.

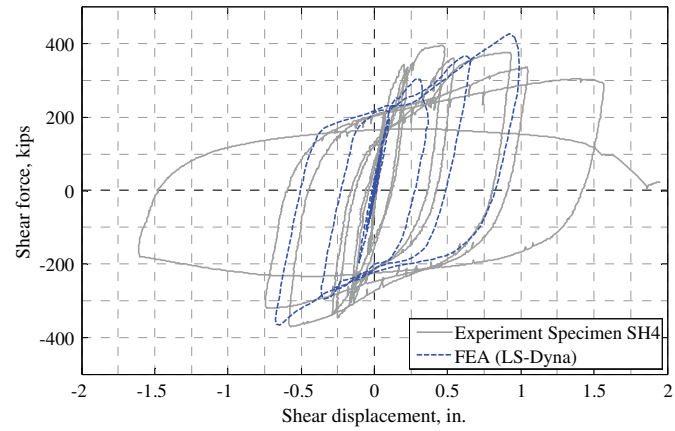

Fig. 3. Finite-element analysis and experimental results comparison for Specimen SH4.

of the flexibility of the components of the test setup, the upper part of the pantograph, including the loading beam and the pantograph diagonals, was modeled together with the shear specimen and the stiffener modules. A complete discussion of the test setup is available in Bruneau et al. (2018).

A half-finite-element model was built taking advantage of the symmetry existing in the test setup. The concrete infill was modeled using constant stress solid elements, and the steel tube was modeled using LS-Dyna's default shell elements (Belytschko-Tsay shell element) with three integration points through the element thickness. A Winfrith concrete material model (MAT085) in LS-Dyna (LSTC 2013) was used for the concrete, and a bilinear elastoplastic material with 1% strain hardening was used for the steel. The average material properties measured by the steel coupon and concrete cylinder tests were used. The contact at the interface of the tube and concrete infill was defined using the Automatic Single Surface Contact algorithm. This contact type is a penalty-based contact, which allows the compression load to be transferred between slave nodes and master segments. The Automatic Single Surface Contact algorithm is a two-way treatment contact, which means that the master and slave nodes are checked for penetration through each other (note that analyses using one-way treatment contact algorithms were also conducted, but those contact elements only check the penetration of slave nodes through the master segments at the contact interface; results from those analyses were unsatisfactory and are not reported here). In the surface contact model used, a friction force develops at the interface when the adjacent parts press on each other and want to slide against each other. A friction coefficient of 0.5 was used at the interface. Sliding will occur when the shear force between the two surfaces reaches the sliding force resistance, which is equal to the compression force at the contact multiplied by a corresponding friction coefficient. No constraints between the concrete fill and the steel tube were used at the ends of the specimen.

The contact between the end surfaces of the specimen's concrete fill and the pantograph's mounting plates was modeled using a similar contact algorithm. The contact between the end edges of the steel tube and the mounting plates was modeled using a node-to-surface contact algorithm, which uses the same contact concept as discussed earlier. The nodes at the edge of the steel tube shell elements and the surface of the mounting plates in contact with the steel tube were assigned to the slave nodes and master surface of the contact algorithm, respectively. A tie contact was used to model all the weld connections in the model. These connections exist between the stiffener plates and the specimen's steel tube. Other details regarding the finite-element modeling of the pantograph, stiffener modules, high-strength bolts, and so forth can be found in Bruneau et al. (2018). To reduce the runtime of the finite-element analyses, the repeated cycles at each nonlinear displacement amplitude in the test loading protocol were not considered in the cyclic displacement history applied to the finite-element model. Note that the test results for the RCFST shafts were generally similar to those for the CFST shear specimen (i.e., Specimen SH4) because the contribution of internal reinforcement to the total shear strength was found to be of little significance. For this reason, finite-element analysis results here are shown only for the CFST shear specimen.

Fig. 3 shows the finite-element results for Specimen SH4 [32.4-cm (12.75-in.)-diameter CFST]. In this figure, the numerically obtained hysteresis curves are compared with the experimental results, with the horizontal axis displaying the shear displacements between two ends of the shear span (i.e., the unstiffened part of the CFTS that is under shear deformations).

As shown in Fig. 3, the initial stiffness of the specimen in the shear span was well matched with the experimentally obtained results. The shear forces were also matched until the cycle in which the experimental shear strength of the specimen was achieved. No failure criteria were defined for the concrete and steel materials, and therefore no failure was exhibited by the finite-element analyses. In fact, in the finite-element analyses, the concrete's strength kept increasing progressively at larger drifts. This increase was consistent with the development of a diagonal compression strut in the concrete. This behavior is observed in Fig. 1.

As shown in this figure, the shear strength for the concrete part given by AASHTO BDS (AASHTO 2014) and WSDOT BDM (WSDOT 2018) is significantly lower than the one given by the finite-element results at the point where the maximum experimental strength is reached. This can be attributed to the fact that, as demonstrated in what follows, the shear strength of the concrete given by these equations does not consider the effect of the compression strut that develops in the concrete under shear deformations. Also, it is observed in Fig. 1(a) that the shear strength of the steel tube given by AASHTO BDS (AASHTO 2014) matches the first yield strength obtained from finite-element analysis, but it underestimates the shear strength contribution of the steel at the maximum experimental strength point. As shown in Fig. 1(b), WSDOT BDM (WSDOT 2018) overestimates the shear strength of the steel tube by about 100% and 50% at the first yield and maximum experimental strength points, respectively.

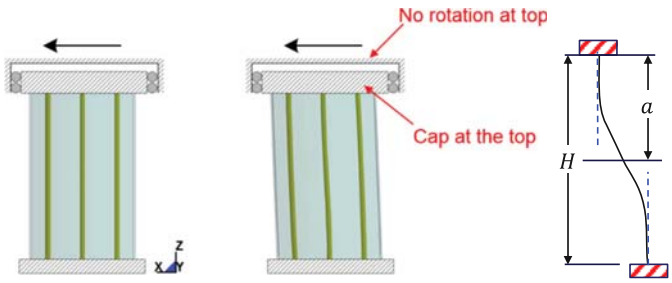

Fig. 4. Loading and boundary conditions for finite-element models.

Proposed Shear Strength Equation

As shown in the previous section, the shear strength values calculated using the WSDOT BDM (WSDOT 2018) equation for the tested RCFST shear specimens were close to the test results. However, the breakdown of the total shear strength into the relative contributions of the steel tube and concrete shows that the WSDOT BDM (WSDOT 2018) equation underestimates the contribution to the total shear strength from the concrete part and overestimates the shear strength provided by the steel tube. The proposed alternative shear strength equation considers the developed compressive diagonal strut in the concrete and its interaction with the steel tube. Note that the potential contribution of the reinforcing cage to the total shear strength is not included in this equation because the effect of the reinforcing cage was shown to have no significant impact on shear strength in the experiments reported by Bruneau et al. (2018).

To investigate the behavior of the RCFST members under shear deformation, a series of finite-element analyses were performed (the developed models did not include reinforcing cages, for the same reason mentioned earlier). Fig. 4 shows a schematic view of the finite-element models developed for the analyses. The finite-element models were developed using the element types and material models of the finite-element models used in the validated finite-element model discussed previously. Taking advantage of the symmetry existing in circular CFSTs under shear deformation, a half-finite-element model was built for the analyses with applied appropriate symmetry boundary conditions. A Winfrith concrete model (MAT085) in LS-Dyna (LSTC 2013) with constant stress solid elements was used for the concrete infill part. The steel tube part was modeled using bilinear elastoplastic material with shell elements with three integration points along the thickness. No strain hardening was assumed for the steel material. The uniaxial compressive strength of the concrete and yield stress of the steel tube were assumed to be 35.9 (5.2) and 399.9 MPa (58 ksi), respectively. The modulus of elasticity of the concrete was calculated according to Section 19.2 of ACI 318 (ACI 2014) as 35,853 MPa (5,200 ksi). The boundary conditions were defined to simulate a double curvature setup, and a monotonically increasing loading was applied at the top. The CFST member was not modeled beyond the shear span. The composite condition was modeled by constraining the slippage between the steel tube and concrete core at both ends of the model. In these regards, the bottom of the model was fixed (i.e., the bottom was not able to move and rotate). This was done by selecting all the nodes at the bottom of the model and fixing the nodes. The constraints at the top of the model were assigned in such a way as to allow side and axial movements but no rotation. This was done by assigning all the nodes at the top of the model to a rigid body constraint with corresponding boundary conditions to fix the rotation. The contact between concrete and steel tube was modeled using normal surface-to-surface contact with a friction coefficient of 0.5. Note that the length of the members above and below the shear

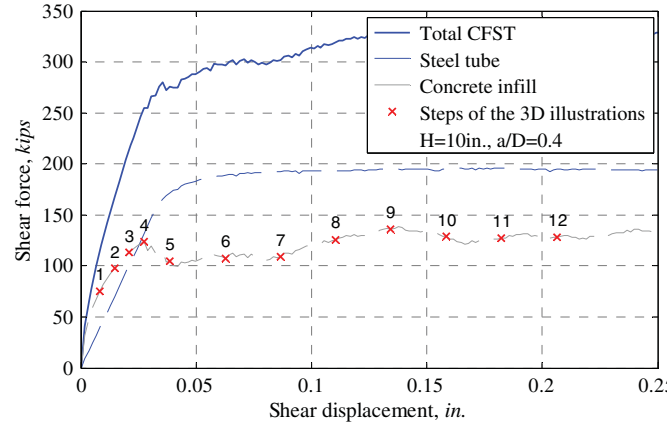

Fig. 5. Shear response of 12OD CFST with $a/D = 0.4$.

zone is sufficient to achieve development of the necessary friction forces between the steel and concrete, except for those instances where such lengths would be nearly nonexistent (Roeder et al. 2016). The finite-element analyses that were conducted on the CFSTs with different shear spans and boundary conditions showed that the development of the compression strut typically depends on the shear span and the composite action of the CFST.

According to the finite-element analyses, three different behaviors can be attributed to the developing compression strut with respect to the CFSTs' shear span-to-concrete-diameter (a/D) ratios. For $a/D < 0.25$, the strut size is governed by the length of the shear span a, while for $0.25 < a/D < 0.5$, it is governed by the diameter of the concrete core. For a/D exceeding 0.5, the strength of the compression strut was not significant and a combined shear-flexural failure type was observed.

Figs. 5–10 show the typical finite-element analysis results for the shear response, expressed by the three-dimensional illustrations of the developing compression strut at various deformations for 30.5-cm (12-in.)-diameter CFSTs for three different a/D values, each of which falls in one of the three different a/D ranges discussed in the previous paragraph. For each a/D value, the first figure shows the relative contribution of the steel and concrete to the total shear strength and identifies the 12 shear displacement values for which three-dimensional illustrations of isosurfaces of the minimum principal stresses in the concrete core are presented in the second figure. The shear displacement was measured as the displacement between the top and bottom of the member under the double curvature loading setup. The minimum principal stress represents the compression field in the concrete. To more clearly illustrate the development of the compression strut, principal stresses lower than 17.2 MPa (2.5 ksi) are not shown in these figures. The range of the plotted minimum principal stresses is shown on the right side of each figure.

Based on the finite-element results, a significant compression strut can be seen to develop in Figs. 6 and 8 for a/D values of 0.4 and 0.12, which fall within the $0.25 < a/D < 0.5$ and $a/D < 0.25$ ranges, respectively. Clearer illustrations of the strut developing in these models are shown in Fig. 11. For both ranges, it was observed that the centerplane of the compression strut passed through the intersection line of a horizontal plane at member's midheight and vertical centerplane that is perpendicular to the direction of the shear loading. This is illustrated in Fig. 11 for the specific examples. The crossing angle is 45°. As shown in these figures, under this assumption the cross-sectional area of the strut is at its maximum at the middle of the height of the member (middle of the free span) and reduces toward both ends of the shear span. Also, it is seen that the stress distribution throughout the strut is not uniform. In fact, the

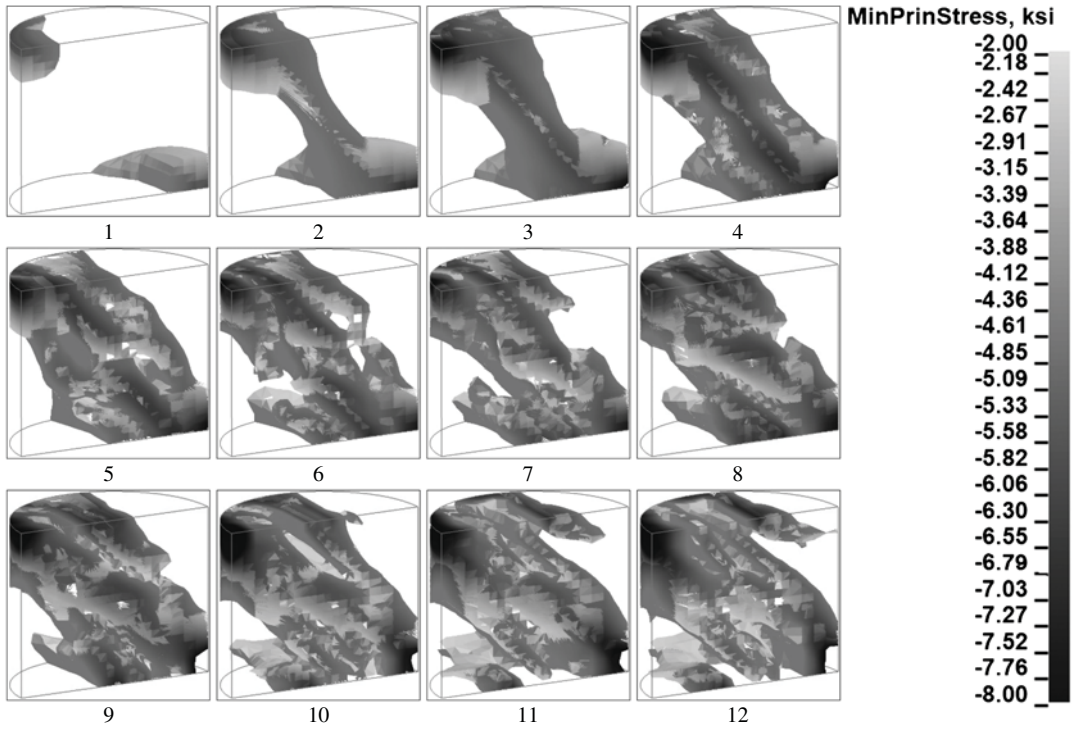

Fig. 6. Three-dimensional illustrations of isosurfaces of minimum principal stresses in concrete core at steps marked in Fig. 5.

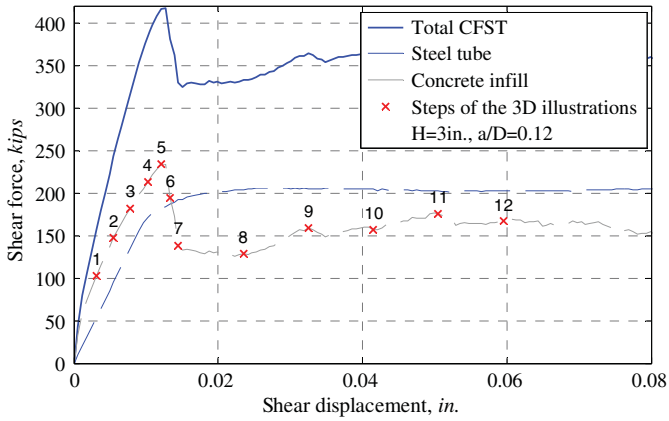

Fig. 7. Shear response of 12OD CFST with $a/D = 0.12$.

compressive stresses are higher at both ends of the strut compared to its middle. This could be attributed to the development of higher confining stresses at both ends of the shear member.

The critical cross section over which the concrete strut is developed can be assumed to be located at the midlength of the strut; a uniformly distributed stress equal to f'_c was assumed to develop in that cross section based on observation of the magnitude of the compressive stresses obtained from the finite-element analyses. Fig. 12(a) shows the definition the critical cross section. This cross-sectional area of the strut (A_{Strut}), from geometry, as shown in Fig. 12(a), can be calculated by Eq. (7):

$$A_{\text{Strut(exact)}} = \frac{\sqrt{2}}{2}\left(4R_c^2 \text{asin}\left(\frac{b}{2R_c}\right) + b\sqrt{4R_c^2 - b^2}\right) \quad (7)$$

where

$$b = \frac{D_c - H}{2}, \quad 0 \le b \le \frac{H}{2}$$

and $R_c = D_c/2$; D_c = concrete core diameter; H = height of specimen in double curvature shear setup, which is equal to $2a$. An approximate simpler formula for the strut cross-sectional area, which was developed by calculating the area of an assumed rectangle that is inscribed inside the strut cross-sectional area, is also given in Eq. (8):

$$A_{\text{Strut(approx.)}} = \sqrt{2}b\sqrt{4R_c^2 - b^2} \quad (8)$$

The strut force F_{Strut} is calculated by multiplying the uniaxial unconfined compressive strength of the concrete by A_{Strut} [Eq. (9)]. The resulting strut force can be decomposed into horizontal and vertical force components, as shown in Fig. 13 and calculated in Eq. (10). The horizontal force component (V_{Strut}) is considered as the shear strength of the strut:

$$F_{\text{Strut}} = f'_c \times A_{\text{Strut}} \quad (9)$$

$$V_{\text{Strut}} = \frac{\sqrt{2}}{2} \times F_{\text{Strut}} \quad (10a)$$

$$P_{\text{Strut}} = \frac{\sqrt{2}}{2} \times F_{\text{Strut}} \quad (10b)$$

In a composite CFST member that is under shear deformation, the vertical force component (P_{Strut}) of the strut transfers to the steel tube as a tensile axial load, as shown in Fig. 13. This P_{Strut} force can be considered a uniform axial compressive and tensile force on the concrete core and the steel tube, respectively.

The shear strength of the concrete core of the CFST (V_{Conc}) when a strut develops is therefore assumed to be equal to V_{Strut}. When no strut develops, the shear strength of concrete can be calculated using the existing shear strength equations developed for the shear strength of the RC members in the absence of strut. Therefore, a lower limit of concrete shear strength (V_c) was defined here for V_{Conc}, as shown in Eqs. (11) and (12). In Eq. (12), the term

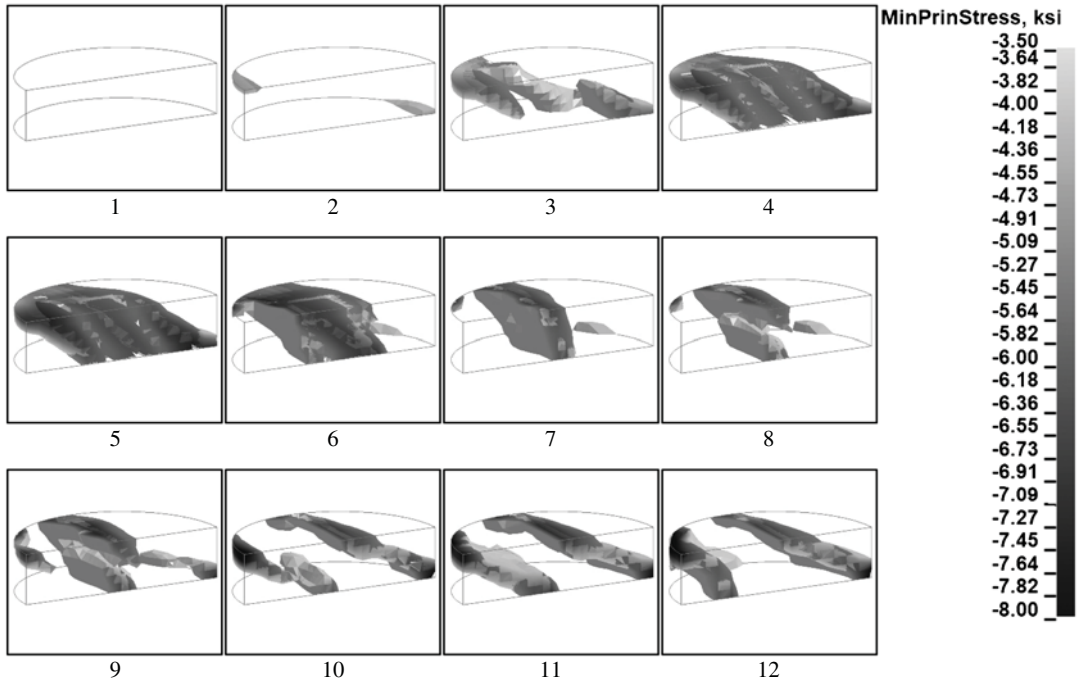

Fig. 8. Three-dimensional illustrations of isosurfaces of minimum principal stresses in concrete core at steps marked in Fig. 7.

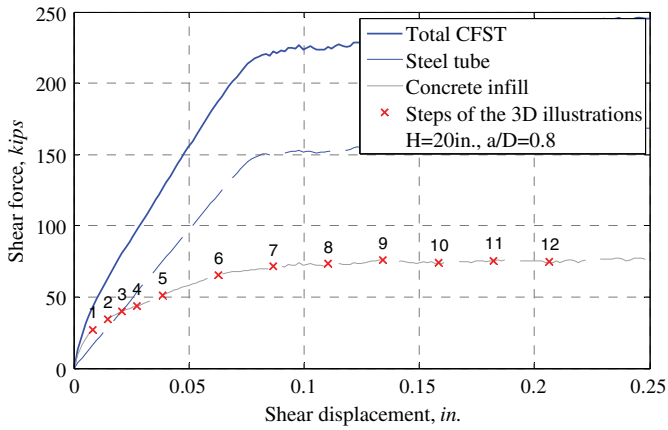

Fig. 9. Shear response of 12OD CFST with $a/D = 0.8$.

outside the parentheses is the nominal shear resistance of the concrete from AASHTO BDS (AASHTO 2014), Article 5.8.3.3. In this equation, β is a "factor indicating the ability of diagonally cracked concrete to transfer tension and shear" and was taken to be equal to 2.0. The term inside the parentheses was added to include the axial load effect on the shear resistance of the concrete. This term was adopted from ACI 318 (ACI 2011, 2014), Article 22.5.6:

$$V_{\text{Conc}} = \max(V_{\text{Strut}}, V_c) \tag{11}$$

where

$$V_c = 0.01286\beta\sqrt{f'_c}A_c\left(1 + \frac{P_{\text{Strut}}}{2A_c}\right) \tag{12}$$

To calculate the nominal shear resistance of the steel tube here, it was assumed that the tube cross section was fully yielded under combined tension and shear, and the effect of bending moment was neglected. In this case, the total shear resistance of the steel tube (V_s) can be calculated by integrating the maximum shear stress (which is tangent to the surface) over the steel tube cross section, as shown in Fig. 14 and calculated in Eq. (13):

$$V_s = 2\int_{-\frac{\pi}{2}}^{\frac{\pi}{2}} \tau_{s,\max} Rt\cos(\phi)d\phi \tag{13}$$

where R = average radius of steel tube; and $\tau_{s,\max}$ = maximum shear stress on steel tube cross section, calculated as

$$\tau_{s,\max} = \frac{1}{\sqrt{3}}\sqrt{F_y^2 - T^2} \tag{14}$$

F_y = yield stress of steel tube; and T = resultant tensile stress on steel tube cross section due to interaction of concrete strut with steel tube (Fig. 13).

The resulting V_s obtained from Eq. (13) is shown in Eq. (15). The term under the square root shows that the shear strength of the steel tube reduces as the strut force increases and P_{Strut} should be less than A_sF_y (for a diagonal strut at 45°$P_{\text{Strut}} = V_{\text{Strut}}$). In other words, the upper limit for the tensile axial load in the steel tube is when the tensile axial load on the steel tube equals the yield strength of the steel tube cross section. This situation is unlikely to happen, but the upper limit was nonetheless considered for the strut force (F_{Strut}) as shown in Eq. (16):

$$V_s = \frac{4Dt}{2\sqrt{3}}\sqrt{F_y^2 - \left(\frac{P_{\text{Strut}}}{A_s}\right)^2} \tag{15}$$

$$V_{\text{Strut}} = P_{\text{Strut}} = \min\left(\frac{\sqrt{2}}{2}f'_c \times A_{\text{Strut}}, A_sF_y\right) \tag{16}$$

Finally, the nominal shear capacity of the composite CFST shaft is taken here as equal to the summation of the shear strength of the concrete core and the steel tube, as shown in Eq. (17). As mentioned earlier, the potential contribution of the reinforcing cage to the total shear strength is not included in this equation:

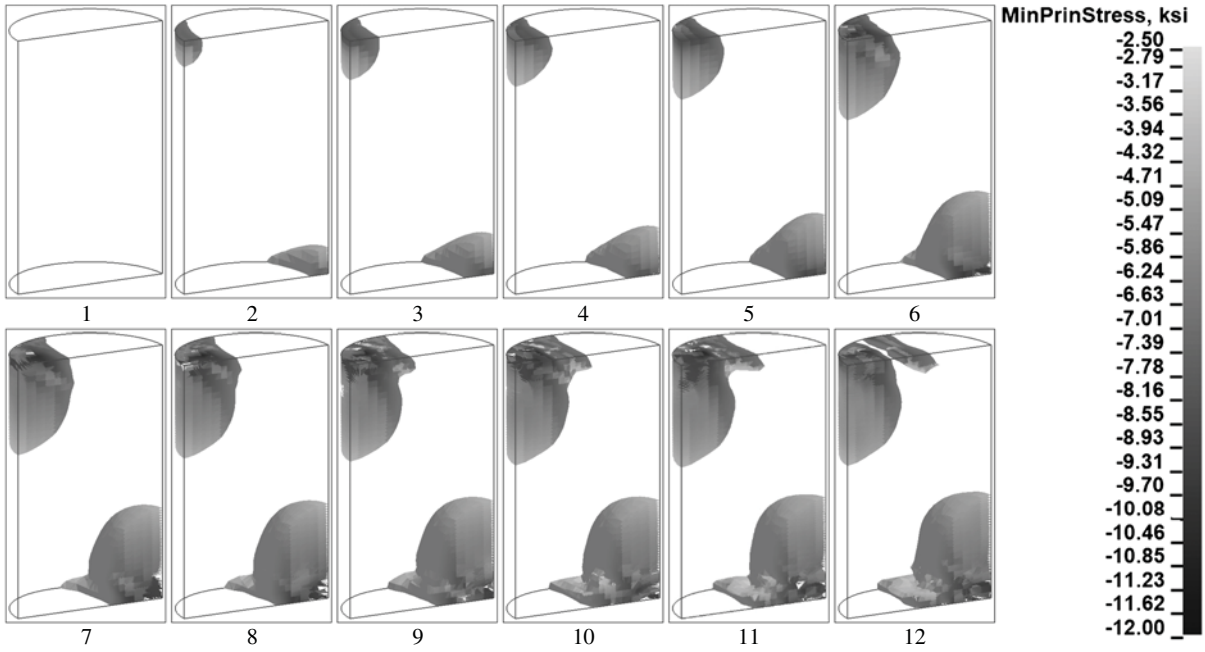

Fig. 10. Three-dimensional illustrations of isosurfaces of minimum principal stresses in concrete core at steps marked in Fig. 9.

$$V_{\text{CFST}} = V_s + V_{\text{conc}} \tag{17}$$

Note that, as mentioned earlier, in the calculation of the shear contribution of the steel tube, the effect of the moment was neglected. In the case of an existing moment on the cross section, such as at the end of the span in the double curvature setup shown in Fig. 4, its effect can be considered in the steel tube shear strength by including the stresses from the bending moment in Eq. (13) as follows:

$$V_{sM} = 2Rt \int_{-\pi/2}^{\pi/2} \frac{1}{\sqrt{3}} \sqrt{F_y^2 - \left(\frac{MR}{I}\sin(\phi) + T\right)^2} \times \cos(\phi) d\phi \tag{18}$$

where M = bending moment on steel tube cross section only; and I = moment of inertia of steel tube cross section. It is assumed that the flexural stresses at the end of span are in the elastic range. Also, the moment carried by the steel tube is equal to $V_{sM} \times H/2$ and the neutral axis is at the center of gravity of the cross section. This assumption was made to solve to the integral of Eq. (18). The contribution of the steel tube in this case is calculated using Eq. (19):

$$\begin{aligned} V_{sM} = \frac{Rt}{\sigma_b\sqrt{3}} \Bigg(& (\sigma_b + T)\sqrt{-\sigma_b^2 - 2\sigma_b T + F_y^2 - T^2} \\ & + F_y^2 \tan^{-1}\left(\frac{\sigma_b + T}{\sqrt{F_y^2 - (\sigma_b + T)^2}}\right) \\ & - (T - \sigma_b)\sqrt{-\sigma_b^2 + 2\sigma_b T + F_y^2 - T^2} \\ & - F_y^2 \tan^{-1}\left(\frac{T - \sigma_b}{\sqrt{F_y^2 - (T - \sigma_b)^2}}\right)\Bigg) \end{aligned} \tag{19}$$

where $\sigma_b = V_{sM}RH/2I$. Eq. (19) is an implicit equation in terms of V_{sm} and needs to be numerically solved using an iterative process. The proposed shear strength in Eq. (17) was compared to finite-element results with different shear-span-to-diameter ratios in Fig. 15.

The proposed shear strength was compared to different steel tube yield strengths, uniaxial compressive strengths of concrete, and different ratios of shear span to diameter (a/D) in Figs. 15 and 16(a and b), respectively. In these figures the vertical axis shows the proposed shear strength divided by the summation of shear yield strength of the steel tube considering no buckling and pure shear strength of concrete fill as calculated by Eqs. (1) and (4), respectively. Also, M_p in Fig. 15 is the composite section plastic moment calculated using the plastic stress distribution method (PSDM). The plastic moment divided by shear span (i.e., M_p/a) is the shear capacity of the member under flexural dominant failure.

Figs. 15(a and b) show the cases in which the bending moment is neglected or it is included in calculating the shear strength, respectively. The difference in the steel tube shear strength between these two cases is less than 8% for $a/D < 0.5$. This difference increases with a/D ratio.

Consideration of External Axial Compressive Load

To account for the effect of an applied external compressive axial load (P_{axial}) on the nominal shear strength of the composite CFSTs, it was assumed that the external load was distributed between the steel tube and the concrete core proportionally to each component's axial stiffness. The portion of the applied P_{axial} that goes to each component is therefore calculated per Eq. (20):

$$P_{\text{axial}} = P_s + P_c \tag{20a}$$

$$P_s - P_{\text{Strut}} \le A_s F_y \quad \& \quad P_c + P_{\text{Strut}} \le f_c' A_c \tag{20b}$$

$$P_s = P_{\text{axial}} \frac{E_s A_s}{E_s A_s + E_c A_c} \le A_s F_y \tag{20c}$$

$$P_c = P_{\text{axial}} - P_s \le f_c' A_c \tag{20d}$$

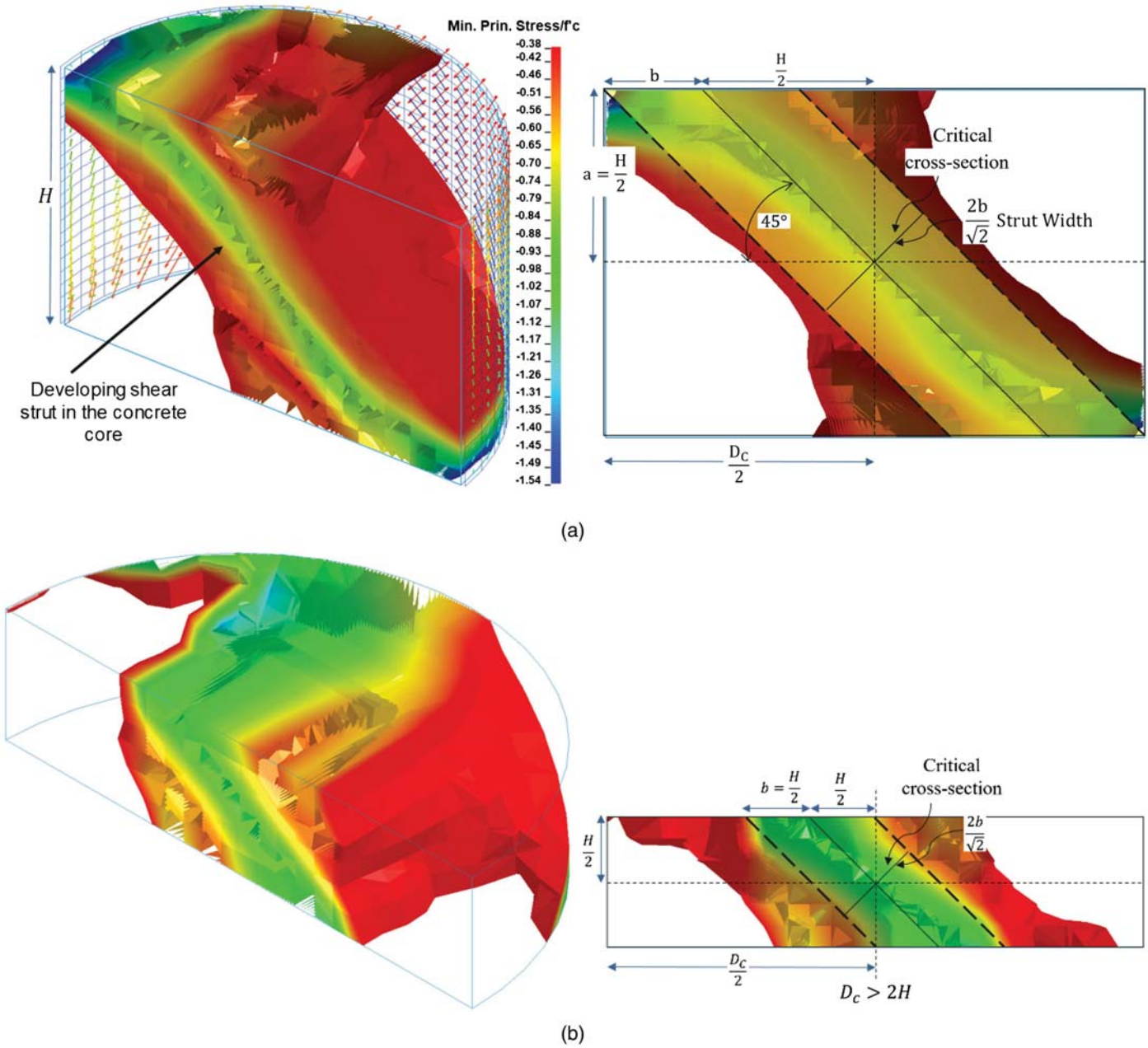

Fig. 11. Definition of diagonal compression strut in RCFST with (a) $0.25 < a/D < 0.5$; and (b) $a/D < 0.25$.

In Eq. (20), P_{axial} = applied axial load on composite section; P_s = proportion of external axial load resisted by steel tube; P_c = proportion of external axial load resisted by concrete infill; E_c = modulus of elasticity of concrete; and other parameters are as defined earlier in the text. Note that the applied load resisted by each component cannot be more than their axial capacity considering no stability effects. This means that P_s and P_c cannot be more than $A_s F_y$ and $f'_c A_c$, respectively.

Considering the applied external axial load on each component, the nominal shear strength of steel tube and the concrete core were modified as shown in Eqs. (21)–(23). Note that the presence of an applied compressive axial load reduces the shear strength of the steel tube and increases the concrete shear strength. In Eq. (23), a factor $\alpha(P_c, A_c)$ is introduced to consider the possible increasing effect of the axial load on the strength of the compression strut, but that effect is neglected in all further calculations here [i.e., $\alpha(P_c, A_c) = 1$]:

$$V_s = \frac{4Dt}{2\sqrt{3}} \sqrt{F_y^2 - \left(\frac{P_{\text{Strut}} - P_s}{A_s}\right)^2} \tag{21}$$

$$V_c = 0.01286\beta\sqrt{f'_c}A_c\left(1 + \frac{P_{\text{Strut}} + P_c}{2A_c}\right) \tag{22}$$

$$V_{\text{Strut}} = P_{\text{Strut}} = \min\left(\frac{\sqrt{2}}{2} f'_c A_{\text{Strut}} \times \alpha(P_c, A_c), A_s F_y + P_s\right) \tag{23}$$

Comparison of Proposed Shear Strength with Experimental Data

The proposed nominal shear strength obtained per the foregoing equations was compared with the results of the tests done by Bruneau et al. (2018) and other researchers (Qian et al. 2007;

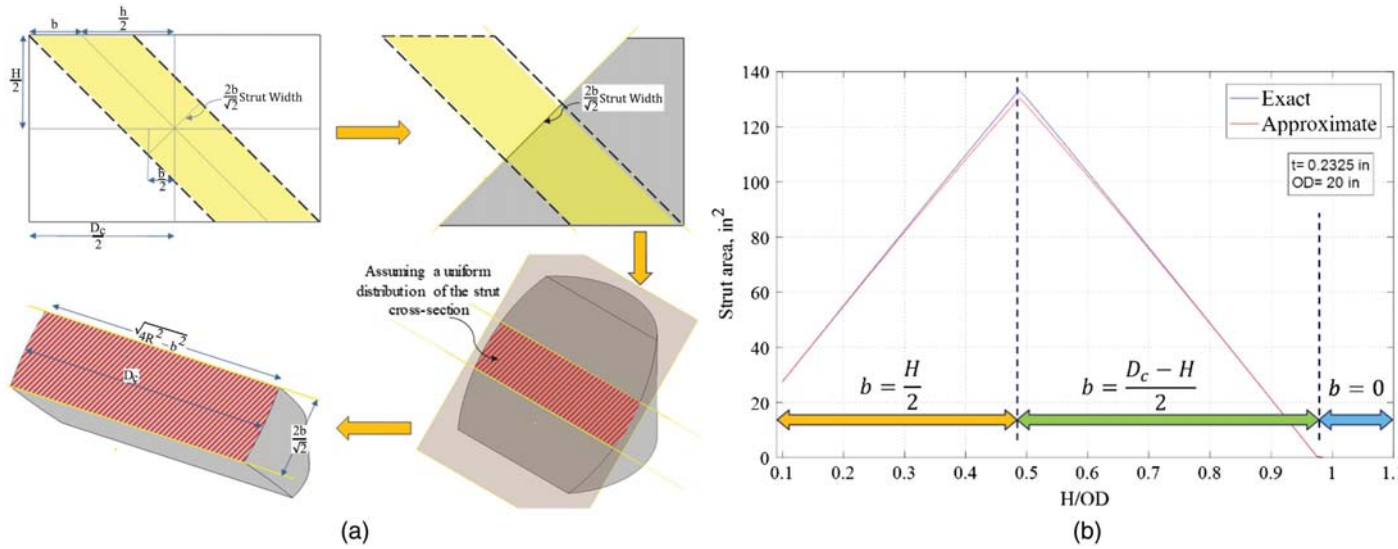

Fig. 12. Cross-sectional area of diagonal compression strut at critical location: (a) definition of area; and (b) comparison of exact and approximate values with respect to span height.

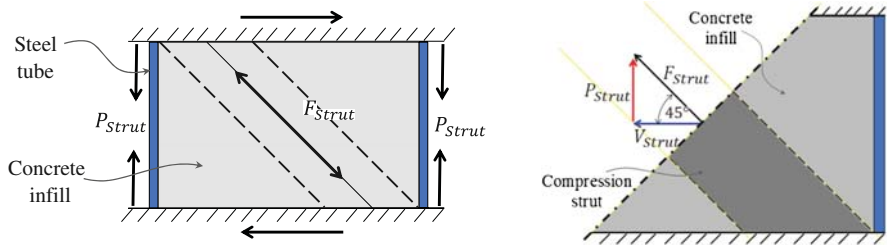

Fig. 13. Horizontal and vertical components of strut force.

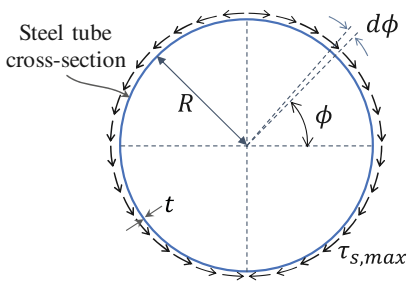

Fig. 14. Shear distribution on steel tube cross section.

Xu et al. 2009; Xiao et al. 2012; Nakahara and Tsumura 2014; Ye et al. 2016; Roeder et al. 2016). Table 3 shows a comparison of the experimentally obtained shear strengths of the specimens tested by Bruneau et al. (2018) with the calculated shear strengths obtained using the proposed equation. For all the RCFST specimens, the experimental values are on average 55%, 7%, and 137% more than the shear strength calculated by the previously proposed formula, WSDOT BDM (WSDOT 2018) and AASHTO BDS (AASHTO 2014), respectively. None of the composite specimens tested by Bruneau et al. (2018) reached their theoretical plastic flexural capacity (M_p). In these tests shear was the governing behavior, and the specimens failed under shear dominant mode. Note that none of the existing test data were tested under a pure shear condition. In fact, there is always a combination of flexure, shear, and axial behavior and failure.

The shear forces carried by the steel tube and the concrete core parts from the finite-element analysis of the tested shear Specimen SH4 were compared to values obtained from the proposed formula in Fig. 17. Comparing the values at the maximum experimental strength point in this figure, the proposed equation gives a good estimate of the shear strength respectively resisted by the steel tube and the concrete compared to WSDOT BDM (WSDOT 2018) and AASHTO BDS (AASHTO 2014), as shown in Fig. 1. Note that both the proposed method and the WSDOT BDM (WSDOT 2018) in particular give a good estimate of the total shear strength of a composite RCFST. However, the WSDOT BDM (2018) does not provide a correct estimate of the shear strength resisted by each individual component of a RCFST.

To further compare with experimental results, the ratios of the shear strength obtained experimentally and obtained using the proposed equation have been calculated for the available data from tests by Qian et al. (2007), Xu et al. (2009), Xiao et al. (2012), Nakahara and Tsumura (2014), Ye et al. (2016), and Roeder et al. (2016) (presented in Tables 4 and 5 for tests without and with axial load, respectively) and Bruneau et al. (2018) (from Tables 2 and 3). Values of this ratio are plotted in Fig. 18 for specimens for which no axial load was applied. Note that values of the experimentally applied moments to the plastic moment, M_{exp}/M_p, included in Tables 4 and 5 show that the values plotted here correspond to specimens that exhibited shear-dominant failures

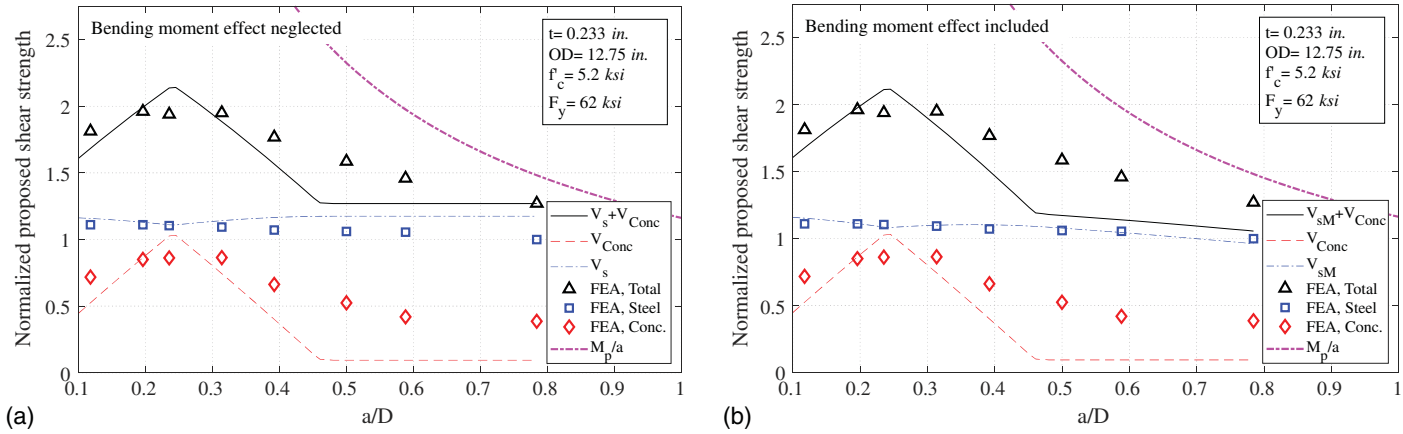

Fig. 15. Normalized proposed shear strength versus shear span to diameter ratios when (a) bending moment effects are neglected; and (b) bending moment effects are included.

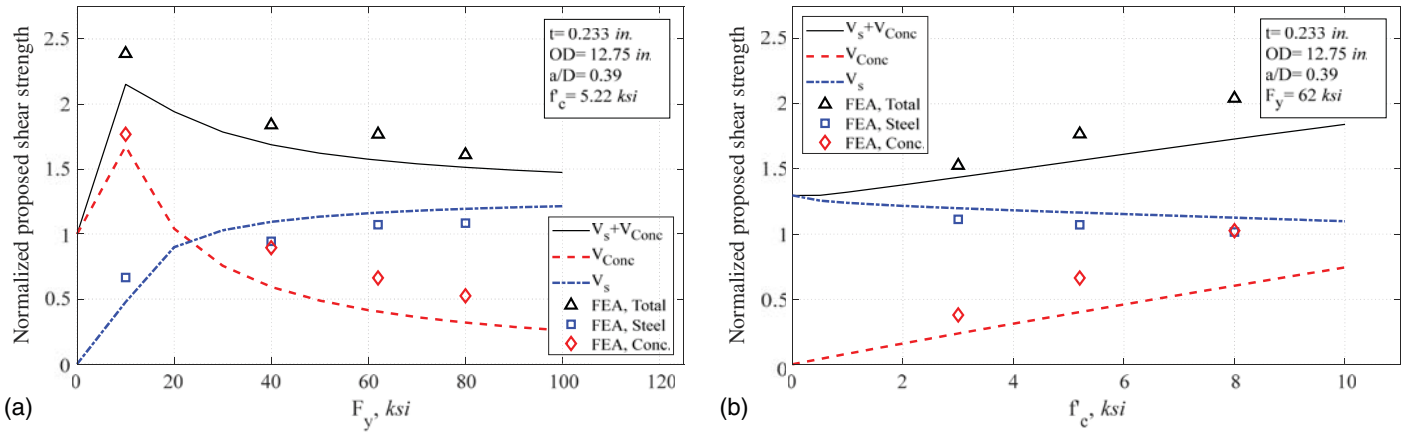

Fig. 16. Normalized proposed shear strength versus (a) yield strength of steel tube; and (b) uniaxial compressive strength of concrete.

Table 3. Comparison of test specimens of Bruneau et al. (2018) with proposed equation

Specimen	V_{exp} (kN)	V_{CFST} (kN)	$\frac{M_{exp}}{M_p}$	$\frac{V_{exp}}{V_{CFST}}$	$\frac{V_{Strut}}{V_{CFST}}$	$\frac{V_s}{V_{CFST}}$	$\frac{V_{conc}}{V_{CFST}}$
SH2	1,943.9	1,214.3	0.83	1.60	0.21	0.79	0.21
SH4	1,761.5	1,156.5	0.80	1.52	0.24	0.76	0.24
SH5	1,765.9	1,156.5	0.73	1.53	0.24	0.76	0.24
SH6	1,841.6	1,156.5	0.69	1.59	0.24	0.76	0.24
SH7	1,810.4	1,156.5	0.75	1.57	0.24	0.76	0.24
SH1R	1,797.1	1,156.5	0.74	1.55	0.24	0.76	0.24

(i.e., not flexure-dominant failures). The maximum calculated ratio of M_{exp}/M_p is 1.2. The horizontal axis in this figure represents the shear-span-to-diameter (a/D) ratio. The mean and standard deviation values of the results are included in the figure. As shown, on average, the experimental values are about 50% more than the values predicted by the proposed formula.

The experimental-to-proposed shear strength ratios for all the available test data, also including specimens for which axial load was applied, are shown in Fig. 19. Fig. 19(a) shows the ratio of experimental to calculated shear strengths versus the applied external axial load, and Fig. 19(b) shows this ratio versus the shear-span-to-diameter ratio. As shown, on average, the experimental values

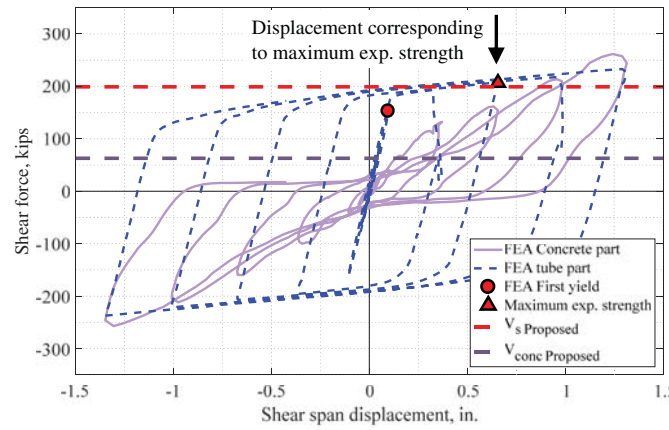

Fig. 17. Comparison of component shear forces of 32.4 cm (12.75 in.) shear specimen (SH4) using proposed formula.

are about 75% more than the values predicted by the proposed formula. According to Fig. 19(a), the proposed formula gives more conservative values for cases with more than $0.5P/P_0$ applied axial load. Also, Fig. 19(b) shows that the predicted values using the proposed formula are more conservative for a/D ratios of less than

Table 4. Existing experimental properties, results, and comparison with proposed equation for tests without axial load

Specimen	OD (cm)	a (cm)	$\frac{a}{OD}$	t (cm)	$\frac{D}{t}$	f'_c (MPa)	E_c, (MPa)	f_y (MPa)	$\frac{P}{P_o}$	P (kN)	$V_{\exp}$ (kN)	V_{CFST} (kN)	$\frac{V_{\exp}}{V_{CFST}}$	$M_{\exp}$ (kN · m)	M_p (kN · m)	$\frac{M_{\exp}}{M_p}$
Roeder et al. (2016)																
R12	50.8	25.4	0.5	0.59	86	42.7	27,793	372	0	0	2,896	1499	1.93	8826	8,421	1.05
R19	50.8	25.4	0.5	0.89	57	62.7	33,723	393	0	0	4,235	2300	1.84	12907	13,129	1.05
R7	50.8	19.1	0.38	0.59	86	44.8	28,345	345	0	0	3,136	2362	1.33	7169	7,899	1.05
R8	50.8	19.1	0.38	0.59	86	44.8	28,414	372	0	0	3,567	2464	1.45	8155	8,450	1.05
R10	50.8	19.1	0.38	0.59	86	42.7	27,676	372	0	0	2,958	2411	1.23	6763	8,415	1.05
R11	50.8	19.1	0.38	0.59	86	45.5	28,696	393	0	0	2,669	2562	1.04	6101	8,882	1.05
R16	50.8	19.1	0.38	0.59	86	59.3	32,750	393	0	0	3,403	2887	1.18	7779	9,071	1.05
R21	50.8	19.1	0.38	0.59	86	0	0	393	0	0	1,997	1357	1.47	4566	6,996	1.05
R14	50.8	12.7	0.25	0.59	86	59.3	32,730	379	0	0	3,674	3772	0.97	5599	8,864	1.05
R15	50.8	12.7	0.25	0.59	86	60.7	33,109	379	0	0	3,541	3683	0.96	5396	8,880	1.05
R20	50.8	12.7	0.25	0.59	86	19.3	18,644	393	0	0	3,167	2411	1.31	4827	8,255	1.05
Ye et al. (2016)																
Ye1	11.9	1.8	0.15	0.20	60	31.7	24,001	338	0	0	240.2	155.7	1.54	52	137	0.38
Ye2	11.9	1.8	0.15	0.20	60	31.7	24,001	338	0	0	240.2	155.7	1.55	53	137	0.38
Nakahara and Tsumura (2014)																
N1	16.5	8.4	0.5	0.49	33.9	64.1	36,791	545	0	0	667.2	533.8	1.25	666	967	0.69
Xiao et al. (2012)																
X1	16.0	6.4	0.4	0.55	29	26.2	21,629	379	0	0	627	423	1.48	480	658	0.73
X2	16.0	6.4	0.4	0.55	29	32.4	24,194	379	0	0	676	432	1.56	518	667	0.78
X3	16.0	6.4	0.4	0.55	29	29.6	23,084	379	0	0	649	427	1.52	499	663	0.75
X4	16.5	6.6	0.4	0.44	38	26.2	21,629	345	0	0	516	343	1.51	408	541	0.75
X5	16.5	6.6	0.4	0.44	38	32.4	24,194	345	0	0	569	356	1.6	450	550	0.82
X6	16.5	6.6	0.4	0.44	38	29.6	23,084	345	0	0	525	347	1.51	416	546	0.76
X7	16.5	6.6	0.4	0.3	55	26.2	21,629	407	0	0	374	289	1.3	297	446	0.66
X8	16.5	6.6	0.4	0.3	55	32.4	24,194	407	0	0	414	303	1.38	328	456	0.72
X9	16.5	6.6	0.4	0.3	55	29.6	23,084	407	0	0	387	294	1.31	305	452	0.68
X25	16.0	2.3	0.14	0.55	29	26.2	21,629	379	0	0	498	467	1.07	132	658	0.20
X26	16.0	2.3	0.14	0.55	29	32.4	24,194	379	0	0	525	485	1.08	138	667	0.21
X27	16.0	2.3	0.14	0.55	29	29.6	23,084	379	0	0	552	476	1.15	145	663	0.22
X28	16.0	2.3	0.14	0.55	29	29.6	23,084	379	0	0	698	476	1.47	184	663	0.28
X29	16.5	2.3	0.14	0.44	38	29.6	23,084	345	0	0	649	391	1.65	179	546	0.33
X30	16.5	2.3	0.14	0.3	55	29.6	23,084	407	0	0	449	338	1.34	125	452	0.28
X31	16.5	2.3	0.14	0.44	38	26.2	21,629	345	0	0	525	383	1.38	145	541	0.27
X32	16.5	2.3	0.14	0.44	38	32.4	24,194	345	0	0	574	405	1.43	159	550	0.29
X33	16.5	2.3	0.14	0.44	38	29.6	23,084	345	0	0	560	391	1.43	156	546	0.28
X34	16.5	2.3	0.14	0.3	55	26.2	21,629	407	0	0	400	325	1.23	110	446	0.25
X35	16.5	2.3	0.14	0.3	55	32.4	24,194	407	0	0	427	347	1.23	118	456	0.26
X36	16.5	2.3	0.14	0.3	55	29.6	23,084	407	0	0	409	338	1.22	113	452	0.25
X55	16.0	8.1	0.5	0.65	25	20	19,057	448	0	0	752	552	1.36	729	884	0.82
X56	16.0	16.0	1	0.65	25	20	19,057	448	0	0	538	552	0.98	1044	884	1.18
X57	16.5	8.4	0.5	0.41	40	20	19,057	407	0	0	440	334	1.33	439	576	0.76
X58	16.5	16.5	1	0.41	40	20	19,057	407	0	0	325	334	0.97	641	576	1.11
Xu et al. (2009)																
Xu16	14.0	1.5	0.1	0.37	38	33.8	24,656	365	0	0	414	276	1.49	69	346	0.20
Xu17	14.0	2.8	0.2	0.37	38	33.8	24,656	365	0	0	369	334	1.11	123	346	0.36
Xu18	14.0	4.3	0.3	0.37	38	33.8	24,656	365	0	0	356	320	1.11	179	346	0.52
Xu19	14.0	7.1	0.5	0.37	38	33.8	24,656	365	0	0	303	231	1.32	255	346	0.74
Xu26	14.0	1.5	0.1	0.37	38	33.8	24,656	365	0	0	391	276	1.41	255	346	0.74
Xu27	14.0	2.8	0.2	0.37	38	33.8	24,656	365	0	0	351	334	1.05	65	346	0.19
Xu28	14.0	4.3	0.3	0.37	38	33.8	24,656	365	0	0	334	320	1.04	118	346	0.34
Qian et al. (2007)																
Q1	19.6	2.0	0.1	0.55	35	40.7	27,041	331	0	0	1,272	547	2.32	294	963	0.31
Q2	19.3	2.0	0.1	0.75	26	40.7	27,041	421	0	0	1,286	845	1.52	298	1,491	0.20
Q7	19.6	3.0	0.15	0.55	35	40.7	27,041	331	0	0	1,953	614	3.17	685	963	0.71
Q8	19.3	3.0	0.15	0.75	26	40.7	27,041	421	0	0	2,037	912	2.23	715	1,491	0.48
Q9	19.6	2.0	0.1	0.55	35	55.8	31,689	331	0	0	2,228	596	3.73	517	1,109	0.47
Q10	19.3	2.0	0.1	0.75	26	55.8	31,689	421	0	0	1,259	894	1.41	292	1,622	0.18
Q15	19.6	3.0	0.15	0.55	35	55.8	31,689	331	0	0	1,023	689	1.49	359	1,109	0.32
Q16	19.3	3.0	0.15	0.75	26	55.8	31,689	421	0	0	1,001	988	1.01	351	1,622	0.22
Q17	19.3	5.8	0.3	0.75	26	55.8	31,689	421	0	0	1,757	1005	1.75	1227	1,622	0.76
Q28	19.6	2.0	0.1	0.55	35	67.6	34,922	331	0	0	1,450	636	2.28	336	1,197	0.28
Q29	19.3	2.0	0.1	0.75	26	67.6	34,922	421	0	0	1,770	934	1.89	409	1,706	0.24
Q34	19.6	3.0	0.15	0.55	35	67.6	34,922	331	0	0	1,286	743	1.73	450	1,197	0.38
Q35	19.3	3.0	0.15	0.75	26	67.6	34,922	421	0	0	979	1045	0.94	343	1,706	0.20

0.2. Note that for the Roeder et al. (2016) tests, the specimens that reportedly had a dominant flexural failure were excluded in the calculation of mean and standard deviation. For the Ye et al. (2016) tests, the specimens with shear-span-to-diameter ratios of less than 0.1 were also excluded in the evaluation of the proposed shear formula. Here, all the other available data for the variety of a/D values were used in evaluating the performance of the proposed equation. However, not all the tested specimens may have had a shear failure

Table 5. Existing experimental properties, results, and comparison with proposed equation for tests with axial load

Specimen	OD (cm)	a (cm)	$\frac{a}{OD}$	t (cm)	$\frac{D}{t}$	f'_c (MPa)	E_c, (MPa)	f_y (MPa)	$\frac{P}{P_o}$	P (kN)	V_{exp} (kN)	V_{CFST} (kN)	$\frac{V_{\text{exp}}}{V_{CFST}}$	M_{exp} (kN · m)	M_p (kN · m)	$\frac{M_{\text{exp}}}{M_p}$
Roeder et al. (2016)																
R13	50.8	19.1	0.38	0.59	86	36.5	25,766	372	0.085	898.5	3,158	2,295	1.38	7,219	8,316	0.87
Ye et al. (2016)																
Ye3	11.9	1.8	0.15	0.2	60	31.7	24,001	338	0.24	142.3	267	160	1.68	58	137	0.42
Ye4	11.9	1.8	0.15	0.2	60	31.7	24,001	338	0.24	142.3	254	160	1.58	54	137	0.40
Ye5	11.9	1.8	0.15	0.2	60	31.7	24,001	338	0.59	346.9	316	156	2.02	69	137	0.50
Ye6	11.9	1.8	0.15	0.2	60	31.7	24,001	338	0.59	346.9	320	156	2.04	69	137	0.50
Ye7	11.9	1.8	0.15	0.2	60	31.7	24,001	338	0.73	431.5	334	151	2.17	72	137	0.53
Ye8	11.9	1.8	0.15	0.2	60	31.7	24,001	338	0.73	431.5	316	151	2.07	69	137	0.50
Ye11	11.9	1.8	0.15	0.2	60	31.7	24,001	338	0.49	289.1	289	160	1.82	62	137	0.46
Ye12	11.9	1.8	0.15	0.2	60	31.7	24,001	338	0.49	289.1	285	160	1.8	61	137	0.45
Ye13	11.9	6.1	0.5	0.2	60	31.7	24,001	338	0.49	289.1	174	107	1.63	126	137	0.92
Ye14	11.9	6.1	0.5	0.2	60	31.7	24,001	338	0.49	289.1	196	107	1.81	140	137	1.02
Ye17	11.9	1.8	0.15	0.2	60	57.2	32,199	338	0.34	289.1	351	214	1.67	76	144	0.53
Ye18	11.9	1.8	0.15	0.2	60	57.2	32,199	338	0.34	289.1	338	214	1.59	73	144	0.51
Ye19	11.9	1.8	0.15	0.3	40	31.7	24,001	414	0.37	289.1	391	236	1.67	84	235	0.36
Ye20	11.9	1.8	0.15	0.3	40	31.7	24,001	414	0.37	289.1	391	236	1.66	84	235	0.36
Nakahara and Tsumura (2014)																
N2	16	7.9	0.5	0.23	70.5	66.2	38,990	503	0.10	182.4	485	249	1.94	465	428	1.08
N3	16.5	8.4	0.5	0.49	33.9	64.1	36,791	545	0.30	774	721	560	1.28	719	967	0.74
N4	16	7.9	0.5	0.23	70.5	66.2	38,990	503	0.30	547.1	427	271	1.58	411	428	0.96
N5	16.5	8.4	0.5	0.5	33	48.3	33,695	545	0.10	226.8	681	547	1.25	679	949	0.72
N6	16.5	8.4	0.5	0.5	33	48.3	33,695	545	0.20	453.7	694	552	1.25	689	949	0.73
N7	16.5	8.4	0.5	0.5	33	48.3	33,695	545	0.40	911.8	658	556	1.19	656	949	0.69
N8	16	7.9	0.5	0.23	70.5	66.2	38,990	503	0.15	271.3	454	254	1.78	435	428	1.02
N9	16	7.9	0.5	0.23	70.5	66.2	38,990	503	0.20	364.7	498	262	1.92	480	428	1.12
Xiao et al. (2012)																
X10	16	6.4	0.4	0.55	29	26.2	21,629	379	0.32	467	730	414	1.76	559	658	0.85
X11	16	6.4	0.4	0.55	29	32.4	24,194	379	0.31	484.8	752	423	1.77	576	667	0.86
X12	16	6.4	0.4	0.55	29	29.6	23,084	379	0.31	471.5	778	418	1.86	599	663	0.90
X13	16.5	6.6	0.4	0.44	38	26.2	21,629	345	0.31	395.9	632	338	1.87	499	541	0.92
X14	16.5	6.6	0.4	0.44	38	32.4	24,194	345	0.30	418.1	654	351	1.87	517	550	0.94
X15	16.5	6.6	0.4	0.44	38	29.6	23,084	345	0.30	400.3	676	343	1.96	534	546	0.98
X16	16.5	6.6	0.4	0.3	55	26.2	21,629	407	0.30	342.5	480	285	1.68	380	446	0.85
X17	16.5	6.6	0.4	0.3	55	32.4	24,194	407	0.28	355.8	485	303	1.61	384	456	0.84
X18	16.5	6.6	0.4	0.3	55	29.6	23,084	407	0.28	342.5	494	294	1.68	392	452	0.87
X19	16	6.4	0.4	0.55	29	26.2	21,629	379	0.64	934.1	703	374	1.89	540	658	0.82
X20	16	6.4	0.4	0.55	29	32.4	24,194	379	0.62	974.1	810	383	2.11	622	667	0.93
X21	16.5	6.6	0.4	0.44	38	26.2	21,629	345	0.62	796.2	649	307	2.11	515	541	0.95
X22	16.5	6.6	0.4	0.44	38	32.4	24,194	345	0.60	836.2	698	325	2.16	555	550	1.01
X23	16.5	6.6	0.4	0.3	55	26.2	21,629	407	0.60	685	547	271	2	431	446	0.97
X24	16.5	6.6	0.4	0.3	55	32.4	24,194	407	0.56	711.7	578	289	2.01	460	456	1.01
X37	16	2.3	0.14	0.55	29	26.2	21,629	379	0.32	467	899	458	1.96	237	658	0.36
X38	16	2.3	0.14	0.55	29	32.4	24,194	379	0.31	484.8	1,001	485	2.07	264	667	0.40
X39	16	2.3	0.14	0.55	29	29.6	23,084	379	0.31	471.5	952	472	2.01	251	663	0.38
X40	16.5	2.3	0.14	0.44	38	26.2	21,629	345	0.31	395.9	823	383	2.17	228	541	0.42
X41	16.5	2.3	0.14	0.44	38	32.4	24,194	345	0.30	418.1	899	405	2.22	248	550	0.45
X42	16.5	2.3	0.14	0.44	38	29.6	23,084	345	0.30	400.3	850	396	2.16	235	546	0.43
X43	16.5	2.3	0.14	0.3	55	26.2	21,629	407	0.30	342.5	676	325	2.07	186	446	0.42
X44	16.5	2.3	0.14	0.3	55	32.4	24,194	407	0.28	355.8	752	351	2.14	207	456	0.45
X45	16.5	2.3	0.14	0.3	55	29.6	23,084	407	0.28	342.5	698	338	2.06	194	452	0.43
X46	16	2.3	0.14	0.55	29	26.2	21,629	379	0.64	934.1	939	423	2.22	248	658	0.38
X47	16	2.3	0.14	0.55	29	32.4	24,194	379	0.62	974.1	1,050	449	2.34	277	667	0.42
X48	16	2.3	0.14	0.55	29	29.6	23,084	379	0.62	938.5	1,201	440	2.73	317	663	0.48
X49	16.5	2.3	0.14	0.44	38	26.2	21,629	345	0.62	796.2	1,023	356	2.87	283	541	0.52
X50	16.5	2.3	0.14	0.44	38	32.4	24,194	345	0.60	836.2	1,050	387	2.73	290	550	0.53
X51	16.5	2.3	0.14	0.44	38	29.6	23,084	345	0.60	800.6	899	374	2.41	248	546	0.45
X52	16.5	2.3	0.14	0.3	55	26.2	21,629	407	0.60	685	765	316	2.42	212	446	0.47
X53	16.5	2.3	0.14	0.3	55	32.4	24,194	407	0.56	711.7	823	343	2.41	228	456	0.50
X54	16.5	2.3	0.14	0.3	55	29.6	23,084	407	0.57	689.4	859	329	2.6	237	452	0.53

Table 5. (*Continued.*)

Specimen	OD (cm)	a (cm)	$\frac{a}{OD}$	t (cm)	$\frac{D}{t}$	f'_c (MPa)	E_c, (MPa)	f_y (MPa)	$\frac{P}{P_o}$	P (kN)	$V_{\exp}$ (kN)	V_{CFST} (kN)	$\frac{V_{\exp}}{V_{CFST}}$	$M_{\exp}$ (kN · m)	M_p (kN · m)	$\frac{M_{\exp}}{M_p}$
							Qian et al. (2007)									
Q3	19.6	2.0	0.1	0.55	35	40.7	27,041	331	0.43	930	1,250	534	2.33	290	963	0.30
Q4	19.3	2.0	0.1	0.75	26	40.7	27,041	421	0.46	1,330	1,668	810	2.06	386	1,491	0.26
Q5	19.6	2.0	0.1	0.55	35	40.7	27,041	331	0.72	1548	1,681	485	3.48	389	963	0.40
Q6	19.3	2.0	0.1	0.75	26	40.7	27,041	421	0.77	2,220	1,819	707	2.58	422	1,491	0.28
Q11	19.6	2.0	0.1	0.55	35	55.8	31,689	331	0.41	1,054	1,210	592	2.04	281	1,109	0.25
Q12	19.3	2.0	0.1	0.75	26	55.8	31,689	421	0.45	1,450	1,232	867	1.42	286	1,622	0.18
Q13	19.6	2.0	0.1	0.55	35	55.8	31,689	331	0.69	1,757	1,495	543	2.76	346	1,109	0.31
Q14	19.3	2.0	0.1	0.75	26	55.8	31,689	421	0.30	965	1,170	890	1.32	271	1,622	0.17
Q18	19.3	5.8	0.3	0.75	26	55.8	31,689	421	0.45	1,450	1,721	996	1.73	1201	1,622	0.74
Q19	19.6	5.8	0.3	0.55	35	55.8	31,689	331	0.69	1,757	1,739	712	2.44	1213	1,109	1.09
Q30	19.6	2.0	0.1	0.55	35	67.6	34,922	331	0.40	1,157	1,672	636	2.63	388	1,197	0.32
Q31	19.3	2.0	0.1	0.75	26	67.6	34,922	421	0.44	1,548	1,205	912	1.33	279	1,706	0.16
Q32	19.6	2.0	0.1	0.55	35	67.6	34,922	331	0.67	1,926	1,005	587	1.71	233	1,197	0.19
Q33	19.3	2.0	0.1	0.75	26	67.6	34,922	421	0.29	1,032	1,294	934	1.39	300	1,706	0.18

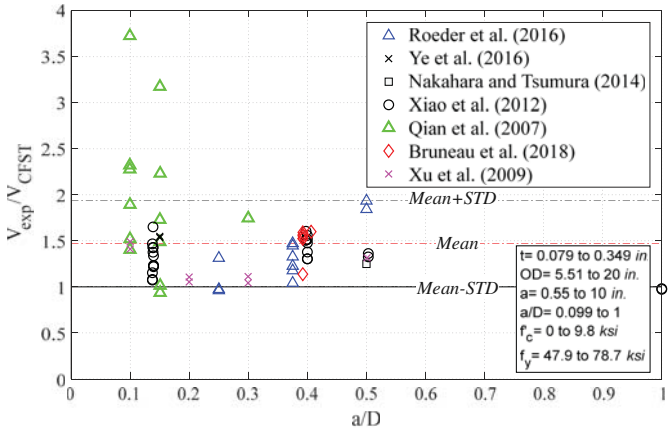

Fig. 18. Ratio of strength from existing test results with no axial load and proposed shear strength formula as a function of shear span, a/D.

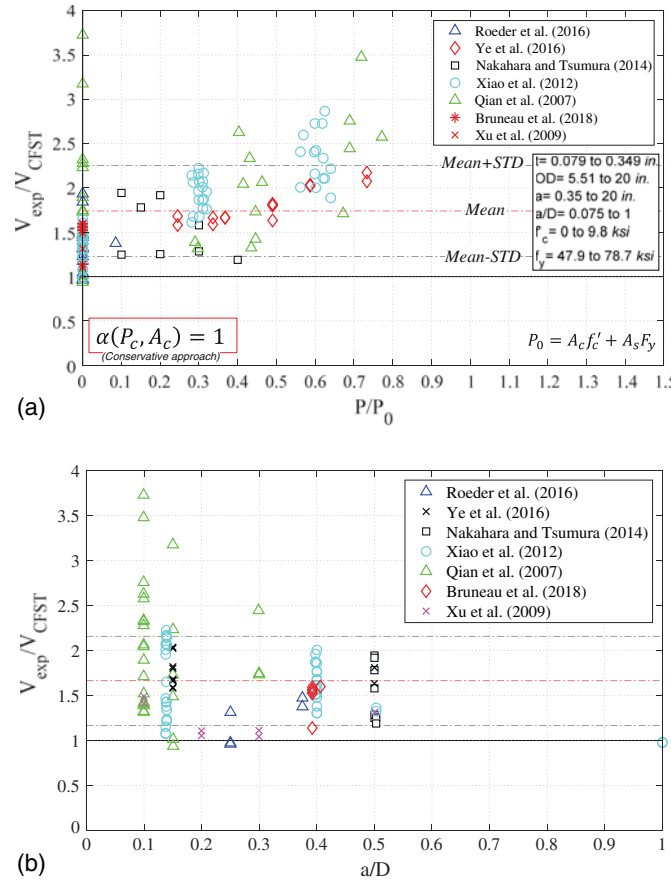

Fig. 19. Ratio of strength from existing test results and proposed shear strength formula as a function of (a) normalized applied axial load, P/P_0; and (b) shear span, a/D.

mode. The test result observations provided by Xiao et al. (2012) and Ye et al. (2016) for tested specimens having a/D values as low as 0.1 and 0.15 suggest that some of those specimens may have had a mixed failure mode of shear combined with other local crushing phenomena. While the results obtained using the proposed equation are safe even when including those results (as shown in Fig. 19), by excluding the test results of $a/D \leq 0.15$, the mean value of experimental-to-proposed shear strengths would improve to 1.59 with a lower standard deviation of 0.32.

Conclusion

Finite-element analysis was used to investigate the shear behavior and ultimate strength of composite RCFSTs. Results showed how a compression strut developed in the presence of low shear spans and provided the basis for developing a proposed equation to quantify the contribution of that strut to total strength as a function of shear span. These results and observations on behavior made it possible to quantify the shortcomings of the shear strength design equation provided by existing design specifications and to develop a proposed mechanics-based shear strength equation for the composite RCFST members that could account for the possible development of a compressive diagonal strut in the concrete and its interaction with the steel tube. The proposed equation accurately captured the contribution of the steel tube to the total strength and conservatively estimated the contribution of the concrete in composite CFSTs. The proposed shear strength equation is based on the governing mechanics in the shear behavior of circular composite members and is not a mathematical fit to the finite-element and test results. The contribution of the steel tube was analytically derived and confirmed with the finite elements. The contribution of the

concrete fill was derived based on a developing strut concept. In the formulation of the strut, its critical cross-sectional area (i.e., the cross section of the strut) was derived based on observations of the behavior of the concrete in the finite-element results. The proposed shear strength formula is a function of the ratio of shear span to diameter, the yield strength of the steel tube, the uniaxial compressive strength of the concrete, and the applied external axial load. It does not distinguish between a shear-dominant failure and the transition from shear-dominant to flexural-dominant failure modes in an explicit way. In fact, it calculates the shear strength corresponding to shear and flexure-shear failure modes based on the values of shear span, yield strength of the steel, and compressive strength of the concrete. The flexural dominant failure happens when the corresponding shear value calculated by dividing the plastic moment strength by the shear span is less than the shear strength calculated by the proposed shear strength formula.

The effectiveness of the proposed equation was compared with shear test data from the existing literature and was found to be safe, with the ratio of experimental to calculated values having a mean value of 1.59 and a standard deviation of 0.32.

Future Research

Future research is desirable, expanding on the procedure used here, to determine the shear behavior and strength of noncomposite members and to establish whether noncomposite RCFSTs can develop a compression strut in the concrete infill under shear deformations. Future research is also desirable to better quantify the shear strength of concrete (in the presence and absence of a compression strut) and the effect of the external axial load so as to further enhance (i.e., reduce the conservativeness) the proposed strength equations. Furthermore, although predicted strengths were compared with results from prior studies, it may be desirable in future research to conduct extensive parametric studies to assess the limits of applicability of the proposed model.

Acknowledgments

This work was sponsored by AASHTO, in cooperation with the Federal Highway Administration (FHWA), and was conducted in the National Cooperative Highway Research Program (NCHRP), which is administered by the Transportation Research Board (TRB) of the National Academies of Sciences, Engineering, and Medicine, under the Research Project NCHRP 12-93. The authors thank the NCHRP 12-93 Program Officer and the other members of the project's advisory panel. However, any opinions, findings, conclusions, and recommendations presented in this report are those of the authors and do not necessarily reflect acceptance by or the views of the National Academy, the TRB, the FHWA, or AASHTO.

References

AASHTO. 2014. *AASHTO LRFD bridge design specifications, customary US Units, with 2015 interim revisions*. 7th ed. Washington, DC: AASHTO.

ACI (American Concrete Institute). 2011. *Building code requirements for structural concrete and commentary*. ACI 318. Farmington Hills, MI: ACI.

ACI (American Concrete Institute). 2014. *Building code requirements for structural concrete: An ACI standard: Commentary on building code requirements for structural concrete (ACI 318R-14): An ACI report*. ACI 318. Farmington Hills, MI: ACI.

AISC. 2016. *Specification for structural steel buildings*. Chicago: AISC.

Brown, N. K. 2013. "Strain limits for concrete filled steel tubes in AASHTO seismic provisions." M.S. thesis, Dept. of Civil, Construction, and Environmental Engineering, North Carolina State Univ.

Bruneau, M., H. Kenarangi, and T. P. Murphy. 2018. *Contribution of steel casing to single shaft foundation structural resistance*. NCHRP Research Rep. No. 872. Washington, DC: Transportation Research Board.

Bruneau, M., and J. Marson. 2004. "Seismic design of concrete-filled circular steel bridge piers." *J. Bridge Eng.* 9 (1): 24–34. https://doi.org/10.1061/(ASCE)1084-0702(2004)9:1(24).

Hajjar, J. F. 2000. "Concrete-filled steel tube columns under earthquake loads." *Prog. Struct. Mater. Eng.* 2 (1): 72–81. https://doi.org/10.1002/(SICI)1528-2716(200001/03)2:1<72::AID-PSE9>3.0.CO;2-E.

Hajjar, J. F., B. C. Gourley, C. Tort, M. D. Denavit, and P. H. Schiller. 2013. "Steel-concrete composite structural systems." Boston: Dept. of Civil and Environmental Engineering, Northeastern Univ. Accessed January 23, 2018. http://www.northeastern.edu/compositesystems.

Han, L. H., and Y. F. Yang. 2005. "Cyclic performance of concrete-filled steel CHS columns under flexural loading." *J. Constr. Steel Res.* 61 (4): 423–452. https://doi.org/10.1016/j.jcsr.2004.10.004.

Lai, Z., A. H. Varma, and K. Zhang. 2014. "Noncompact and slender rectangular CFT members: Experimental database, analysis, and design." *J. Constr. Steel Res.* 101 (Oct): 455–468. https://doi.org/10.1016/j.jcsr.2014.06.004.

Leon, R. T., D. K. Kim, and J. F. Hajjar. 2007. "Limit state response of composite columns and beam-columns Part I: Formulation of design provisions for the 2005 AISC specification." *Eng. J.* 44 (1): 341–358.

LSTC (Livermore Software Technology Corp.). 2013. *LS-DYNA keyword user's manual version R7.0*. Livermore, CA: LSTC.

Marson, J., and M. Bruneau. 2004. "Cyclic testing of concrete-filled circular steel bridge piers having encased fixed-based detail." *J. Bridge Eng.* 9 (1): 14–23. https://doi.org/10.1061/(ASCE)1084-0702(2004)9:1(14).

Moon, J., D. E. Lehman, C. W. Roeder, and H. E. Lee. 2013. "Strength of circular concrete-filled tubes with and without internal reinforcement under combined loading." *J. Struct. Eng.* 139 (12): 04013012. https://doi.org/10.1061/(ASCE)ST.1943-541X.0000788.

Nakahara, H., and R. Tsumura. 2014. "Experimental study on shearing behavior of circular CFT short column." *J. Struct. Constr. Eng.* 79 (703): 1385–1393. https://doi.org/10.3130/aijs.79.1385.

Qian, J., Y. Cui, and X. Fang. 2007. "Shear strength tests of concrete filled steel tube columns." *Tumu Gongcheng Xuebao (China Civ. Eng. J.)* 40 (5): 1–9.

Roeder, C., D. Lehman, and E. Bishop. 2010. "Strength and stiffness of circular concrete-filled tubes." *J. Struct. Eng.* 136 (12): 1545–1553. https://doi.org/10.1061/(ASCE)ST.1943-541X.0000263.

Roeder, C., D. Lehman, and A. Maki. 2016. *Shear design expressions for concrete filled steel tube and reinforced concrete filled tube components*. Washington, DC: Washington State DOT.

WSDOT (Washington DOT). 2018. *Bridge design manual LRFD*. Olympia, WA: WSDOT.

Xiao, C., S. Cai, T. Chen, and C. Xu. 2012. "Experimental study on shear capacity of circular concrete filled steel tubes." *Steel Compos. Struct.* 13 (5): 437–449. https://doi.org/10.12989/scs.2012.13.5.437.

Xu, C., L. Haixiao, and H. Chengkui. 2009. "Experimental study on shear resistance of self-stressing concrete filled circular steel tubes." *J. Constr. Steel Res.* 65 (4): 801–807. https://doi.org/10.1016/j.jcsr.2008.12.004.

Ye, Y., L.-H. Han, Z. Tao, and S.-L. Guo. 2016. "Experimental behaviour of concrete-filled steel tubular members under lateral shear loads." *J. Constr. Steel Res.* 122 (Jul): 226–237. https://doi.org/10.1016/j.jcsr.2016.03.012.